

Triboplasma Generation and Triboluminescence: Influence of Stationary Sliding Partner

Keiji Nakayama

Received: 27 August 2008 / Accepted: 27 August 2009 / Published online: 11 September 2009
© Springer Science+Business Media, LLC 2009

Abstract In this work, the characteristics of triboplasma have been investigated from the point of view of how the kinds of the stationary partner influence the photon energy and the plasma distribution. The energy spectrum and two-dimensional images of the emitted photons were measured during the sliding of a diamond pin with a tip radius of 1.5 and 3 mm on the three kinds of disk made of Al_2O_3 , MgO , and SiO_2 in dry sliding in air. The results showed that all the three kinds of solid tested had narrow bands of air-discharge plasma in the ultraviolet region, demonstrating that the triboplasma generation does not depend on the kinds of insulating solids. Triboplasma was distributed having a ring with one or two tails in all the three kinds of solid Al_2O_3 , MgO , and SiO_2 . The mechanisms of UV, visible, and IR photon emissions are discussed. The UV photons are emitted from the ionized plasma gas produced by discharging of air, while the visible photons are emitted from the defect and impurity centers excited by the triboplasma-photons, triboplasma-electrons, and frictional temperature rise together with the photons from the plasma itself. A 696-nm narrow band appeared only with Al_2O_3 , and it was attributed to the Cr^{3+} ions excited by the UV photons and electrons from the triboplasma. The IR photons should be emitted from the sliding contact by the thermal emissions consisting of thermoluminescence and blackbody radiation, as well as from the triboplasma. The

visible photon emission was strongest at the pair points facing across the frictional track in Al_2O_3 and MgO . To explain the photon emission at the pair points, a new model has been proposed, in which the visible photons are emitted from the surface defect and/or impurity centers excited by the back electrons accelerated with the inverse electric field caused by the negatively charged patches produced by the electron bombardment to the diamond surface. The negative charges on the frictional track repelled the back electrons, so that the back-electrons attack just outside the frictional track.

Keywords Triboplasma · Photon energy · Diamond · Aluminum oxide · Magnesium oxide · Silicon oxide · Luminescence · Photoluminescence · Cathodoluminescence · Thermoluminescence

1 Introduction

Chemical reactions under lubrication have mainly been explained so far by frictional temperature rise [1] combined with catalytic action [2, 3], since a flash temperature was observed [4]. However, various chemical reactions, termed tribochemical reactions, remain without being explained by this traditional mechanism [5]. Several mechanisms have been proposed to explain the reactions, those caused by freshly worn surface [6], by the attachment of low-energy electrons emitted from worn surfaces [7], by the shearing of molecules [8], and so on, but even so, it is still difficult to fully explain tribochemical reactions. This is because, for example, engineering sliding surfaces are in mild wear regions covered with oxide films or DLC films and number of low-energy electrons is too small to cause substantial reactions [9], and the role of shearing reactions is still not

K. Nakayama (✉)
Chiba Institute of Technology, 2-17-1, Tsudanuma,
Narashino-shi, Chiba 275-0016, Japan
e-mail: keiji.nakayama@it-chiba.ac.jp

K. Nakayama
National Institute of Advanced Industrial Science and
Technology (AIST), 1-2-1, Namiki, Tsukuba-shi,
Ibaraki 305-8564, Japan

clear because there is no good tool to investigate in situ the molecular shearing phenomena inside the sliding contact area, so a simulation study for this is anticipated [10].

On the other hand, enormous numbers of high-energy electrons [11], negative and positive ions [12], and high-energy ultraviolet photons [13, 14] are emitted during sliding in various solids especially insulating solids. The phenomena are called “triboemission,” the intensity of which depends greatly on the electric resistivity of the sliding partners [13, 14]. Further, the ratio of intensity of emitted electrons to that of positive ions decreases with the electric resistivity of a solid approaching the minimum value of one in insulators, where the same number of electrons and positive ions are emitted [13, 14]. It was thereby concluded that plasma is generated in the vicinity of the sliding contact in insulators, since it is “a highly ionized gas in which the charge of the electrons is balanced by the charge of the positive ions, so that the system as a whole is electrically neutral” [15]. Based on this systematic work, a model of triboplasma generation was proposed in 1996 [16]. The predicted plasma was discovered in the rear gap of the sliding contact in dry sliding in 2001 [17] and then under-oil lubricated sliding conditions in 2006 [18]. As it is known that high-energy state of plasma causes plasma reactions, triboplasma should be one of the main causes of tribochemical reactions in insulators and semiconductors [19, 20].

Plasma generation has been explained by the discharge of ambient gas molecules emitting ultraviolet photons through an electron avalanche process by intense electric fields caused by tribocharging or triboelectrification [13, 14, 21]. The size and intensity of triboplasma depend greatly on sliding conditions [18], gas pressures [22], gas species [23], and the geometry of the sliding partners [24]. The intensity of triboplasma generation and in turn triboemission intensity, which is emitted from triboplasma, increase in the order of insulator > semiconductor > conductor (metals) [13, 14]. The energy of electrons emitted from the sliding contact also increases in this order of insulator > semiconductor > conductor [11]. This is because tribocharging or triboelectrification, which cause

triboplasma, increases in this order, i.e., with an increase in electric resistivity.

Several kinds of tribocharging mechanisms have been proposed so far. They are (1) work function difference between contacting solids [25], (2) asymmetric rubbing, where a smaller sliding partner is heated up more than a larger partner [26], (3) charging by transfer of protons or hydroxides [27], (4) wearing down of a neutralized surface layer to expose an intrinsic charged surface [28], and so on. As tribocharging or triboelectrification is deeply concerned with solid species [25], triboplasma generation should also be deeply concerned with sliding solid species. Generally, sliding partners are composed of stationary and moving components as in piston-ring/liner, cam/tappet, shaft/bearings, and so on. So both relative size and type of solid species of the sliding partner should affect triboelectrification and, in turn, triboplasma generation.

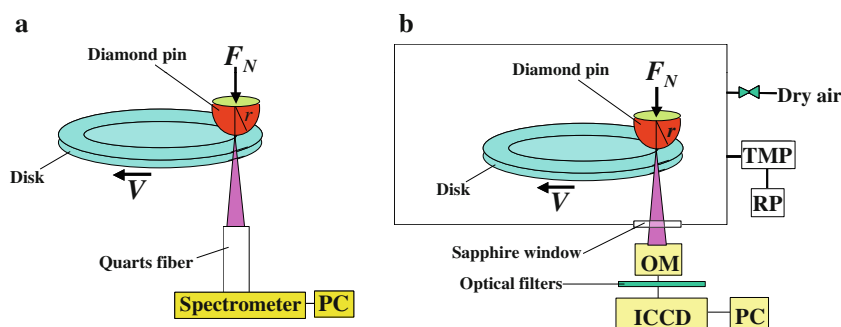
In this work the author investigated triboplasma generation in relation to the kinds of solid of a stationary sliding partner. The results showed that the photon energy spectrum and plasma distribution greatly depend on the kinds of solid of stationary sliding partners. The mechanisms of photon emission have been discussed.

2 Experimental Procedures

Figure 1a shows an apparatus to measure the energy spectrum of photons emitted while sliding a diamond pin against a rotating disk in ambient air in the dark. The diamond had a tip radius of $r = 1.5$ mm and the disks were made of single-crystal aluminum oxide (sapphire, Al_2O_3), single-crystal magnesium oxide (MgO), and single-crystal silicon oxide (quartz, SiO_2). The photon energy spectrum was measured for Al_2O_3 under a normal force of $F_N = 1.0$ N in ambient air at relative humidity of $\text{RH} = 40\%$, while it was measured for MgO and SiO_2 under $F_N = 1.50$ N in ambient air at $\text{RH} = 72\%$. All sliding experiments were performed under a sliding velocity of $V = 32$ cm/s.

Figure 1b shows an apparatus to measure two-dimensional images of photons emitted while sliding a diamond

Fig. 1 Apparatuses to measure energy spectrum (a) and two-dimensional images (b) of photons emitted during sliding a diamond pin against a rotating disk in air, where OM is optical microscope, ICCD is intensified charge-coupled device, PC is personal computer, TMP is turbo-molecular pump, and RP is rotary pump



pin with tip radiuses of $r = 1.5$ and 3.0 mm against the above mentioned three kinds of rotating disks (Al_2O_3 , MgO , and SiO_2) in dry air, using an ICCD camera after magnification with an optical microscope (OM). By inserting filters, which allow passage of UV, visible, 696-nm, and IR photons between the OM and ICCD camera, UV, visible, 696-nm, and IR photon images were taken, which have transmission wavelength regions of 290–420 nm, 400–800 nm, 696 ± 10 nm, and 800–2500 nm, respectively. The ICCD camera detects the photon energies ranging from 200 to 900 nm. All sliding experiments were performed under $V = 32$ cm/s and $F_N = 0.5$ N in dry air in the dark. The diamond pins used were made of natural diamond, which contains normally no detectable impurities by the information from the firm. According to the data from the firm, the main impurities in the crystal Al_2O_3 (sapphire) disk were $\text{Ba} < 0.1$, $\text{Ca} < 0.1$, $\text{Cr} < 2$, $\text{Cu} < 2$, $\text{Fe} < 1$, $\text{K} < 1$, $\text{Mg} = 0.1$, $\text{Mn} < 0.5$, $\text{Na} < 1$, $\text{Si} < 10$, $\text{Sr} < 0.1$, $\text{Ti} < 10.6$, $\text{Zn} < 2$, $\text{Zr} < 1$ in ppm, whereas those in the crystal MgO disk were $\text{Ca} = 20$, $\text{Si} < 10$, $\text{Al} = 130$, $\text{Fe} = 140$, $\text{B} < 10$ in ppm, and those in crystal SiO_2 disk were < 0.1 ppm for all elements measured. Due to the information from the firm, the surfaces of the Al_2O_3 and MgO disks were finished with mechanochemical polishing using silica SiO_2 abrasive particles, whereas the surface of the MgO disk was finished with ceria, CeO_2 .

The experimental conditions for measuring the energy and images are summarized in Table 1.

3 Results

3.1 Al_2O_3

Figure 2a shows the spectrum of photons emitted while sliding a diamond pin with $r = 1.5$ mm on an Al_2O_3 single-crystal disk in the ambient air, which is composed of several narrow bands in the ultraviolet region, a narrow band at 696-nm and weak photon emission in the wavelength region 400–700 nm, and a broad band in the wavelength region 700–900 nm where the peak position is not clear. On the

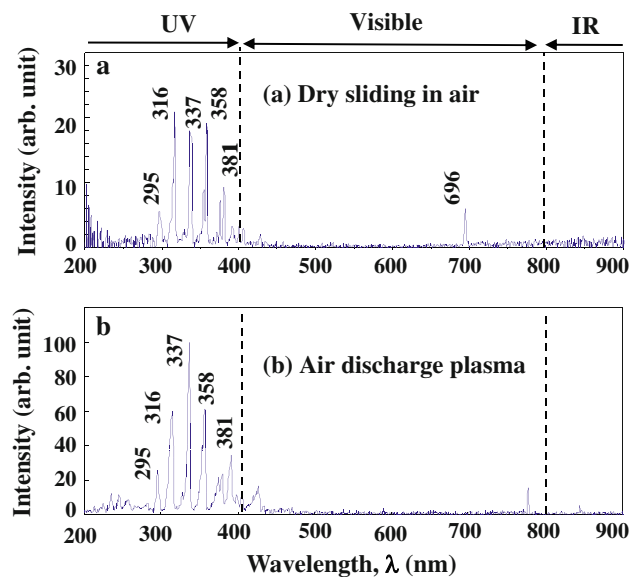


Fig. 2 Energy spectrum of photons emitted during sliding of a diamond pin with a tip radius of $r = 1.5$ mm on a rotating Al_2O_3 disk under $F_N = 1.0$ N and $V = 32$ cm/s in ambient air with a relative humidity of $\text{RH} = 40\%$ (a) and that emitted from the air-discharge plasma between a steel needle and a steel flat disk at an electrode distance of 0.3 mm in ambient air with $\text{RH} = 40\%$ (b)

other hand, Fig. 2b shows the spectrum of photons emitted from the discharge of dry air between a steel needle and a steel plate at an electrode distance of 0.3 mm in the ambient air with a relative humidity of 40%. It is seen that the photon spectrum in the UV region in the tribophoton and air-discharge photon completely coincides, confirming that the triboplasma is generated through the discharging of air in the gap of sliding contact [13, 14]. The origin of the 696-nm peaks in Fig. 2a will be discussed below. A narrow band in the wavelength region 750–800 nm in the air-discharge plasma is noise.

Figure 3 (top) shows optical microscopic images of the contact points measured under $F_N = 1.0$ N after a sliding experiment in light illumination, while Fig. 3 (middle) shows the *effective* two-dimensional images measured during sliding in the dark, which are displayed by camera auto-contrast mode, and Fig. 3 (bottom) shows the

Table 1 Experimental conditions

	Tip radius, r , of diamond pin (mm)	Disk	Normal force, F_N	Sliding velocity, V	Atmosphere
Energy spectrum	1.50	Al_2O_3	1.0 N	32 cm/s	Ambient. air, 40%
	1.50	MgO	1.5 N	32 cm/s	Ambient. air, 72%
	1.50	SiO_2	1.5 N	32 cm/s	Ambient. air, 72%
Photon image	1.50	Al_2O_3	0.5 N	32 cm/s	Dry air
	1.50	MgO	0.5 N	32 cm/s	Dry air
	1.50	SiO_2	0.5 N	32 cm/s	Dry air
	3.00	SiO_2	0.5 N	32 cm/s	Dry air

maximum two-dimensional images also measured in the dark, where weak photon emissions in the peripheral zone in the effective images are displayed to the maximum level, for UV, Visible, 696-nm, and IR photons emitted during sliding, in the tribosystem of a diamond pin with a tip radius of $r = 1.5 \text{ mm}$ on an Al_2O_3 disk under $F_N = 0.5 \text{ N}$ and $V = 32 \text{ cm/s}$. The color shows the photon intensity levels in the order of red > yellow > green > blue > black = 0. The black area in the bottom figure shows the photon intensity beyond the red level, which is 10 counts/pixel in all bottom figures in Fig. 3.

In this sliding experiment, wear was negligibly small, so the optical images gave a clear circular Hertzian contact area even after the sliding experiment, as seen in the top figures. It is seen that triboplasma is distributed in the rear part of the sliding contact, having an elliptical ring in all four kinds of images. Only the 696-nm photon image showed a tailing in the effective images, while all the maximum images showed a tailing except the UV image.

To know the relative size of the effective and maximum plasma zone, the effective plasma images were overlapped onto the maximum ones except for the 696-nm image to give Fig. 4. For the 696-nm image, the effective and maximum images are shown in Fig. 4c and d, separately, without overlapping, because the sizes of both images are almost the same. In the UV and visible images, the maximum plasma zone is spread out in a much wider area than the effective zone as seen in Fig. 5a and b, while in the IR image, the difference between the effective and maximum plasma zones is small, with slightly greater size in the maximum one. One question arises. Does the plasma really spread to such a broad area expressed by the maximum

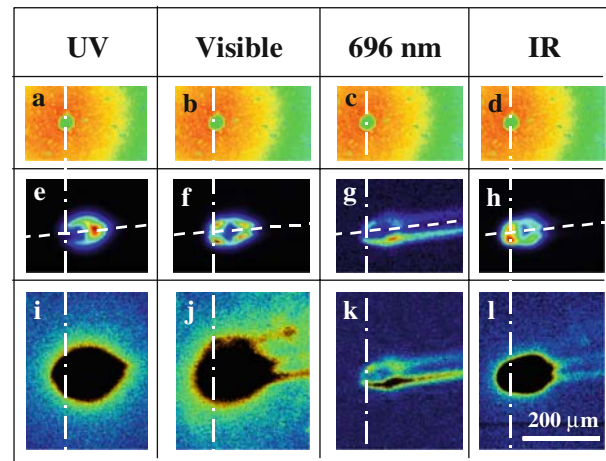
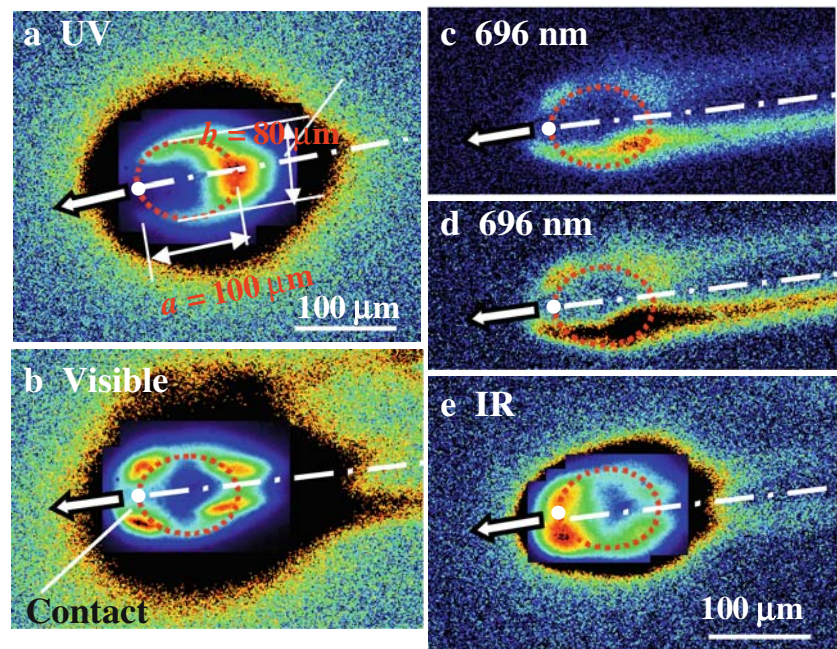


Fig. 3 Top figures show optical microscopic images of the contact after the sliding experiments under light illumination, middle figures and bottom figures show effective and maximum two-dimensional images, respectively, of photons emitted during sliding of a diamond pin with a tip radius of $r = 1.5 \text{ mm}$ on a rotating Al_2O_3 disk under $F_N = 0.5 \text{ N}$ and $V = 32 \text{ cm/s}$ in dry air in the dark. The color shows the photon intensity level in the order of red > yellow > green > blue > black = 0 in the middle and bottom images. The black zone surrounded by red in the bottom maximum images shows the intensity beyond the red = 10 counts/pixel

zone as seen in the UV and visible images [24]? As it is well known that photons with shorter wavelength have a higher-scattering nature, there is a possibility that the broad area in the maximum images of UV and visible photons is the result of the high-scattering nature. However, we need further work to come to conclusion on this matter.

In this experiment, the plasma ring was not a circle [17] but an elliptical ring [24] having major axis $a = 100 \text{ μm}$

Fig. 4 Composite images (a, b, and e), where the effective images are overlapped onto the maximum images, and effective (c) and maximum (d), images of 696-nm photons under the same experimental condition as in Fig. 3



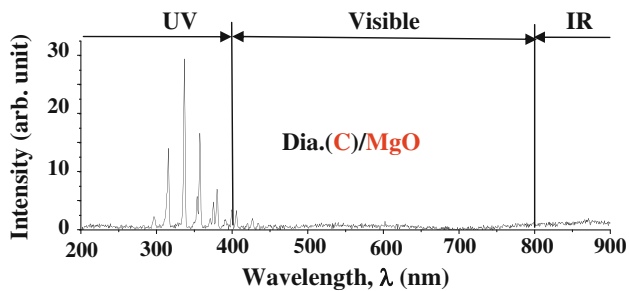


Fig. 5 Energy spectrum of photons emitted during sliding of a diamond pin with a tip radius of $r = 1.5$ mm on a rotating MgO disk under $F_N = 1.0$ N and $V = 32$ cm/s in ambient air with RH = 72%

and minor axis $b = 80$ μm , elongated a little bit in the direction of sliding. The UV photon intensity is most intense at the crossing point of the plasma ring and the wear track, i.e., at the center of the plasma horseshoe pattern. The gap distance of the two sliding surfaces at the crossing point was $d_T = 3.3$ μm . However, in the visible, 696-nm, and IR photons, the emission intensities were high at the two kinds of pair points facing each other across the wear track at the sliding contact and the center of the plasma horseshoe. It is seen that the tailings are originated from the two pair points in visible, 696-nm, and IR photon images. The photons from the tailing in 696-nm photons have been thought to be emitted from the surface atoms excited by the active particles such as UV photons, and electrons produced in the triplasma. [13, 14]. This suggests that the tailings in the visible and IR images are also caused by the same mechanism. The emission mechanism of visible, 696-nm, and IR photons will be discussed below.

3.2 MgO

Figure 5 shows the energy spectrum of photons emitted while sliding a diamond pin with a tip radius of $r = 1.5$ mm against an MgO single-crystal disk. In this case, several narrow plasma bands also appeared in the ultraviolet region, which corresponded to those of the air-discharge plasma shown in Fig. 2b, demonstrating that gas-discharge triplasma is generated also in MgO. However, no narrow band at 696-nm, which was observed in Al_2O_3 , appeared in MgO. Instead of the narrow band at 696-nm, weak broad bands appeared in both the visible and IR regions. This means that the narrow band at 696-nm can be attributed to the solid surface of Al_2O_3 .

Figure 6a shows an optical microscopic image of the contact under $F_N = 0.5$ N after the sliding experiment in light illumination, while the Fig. 6b and c shows the effective total photon image and composite total photon image, respectively, during the sliding of a diamond pin with a tip radius of $r = 1.5$ mm against an MgO single-crystal disk under $F_N = 0.5$ N and $V = 32$ cm/s. In Fig. 6c,

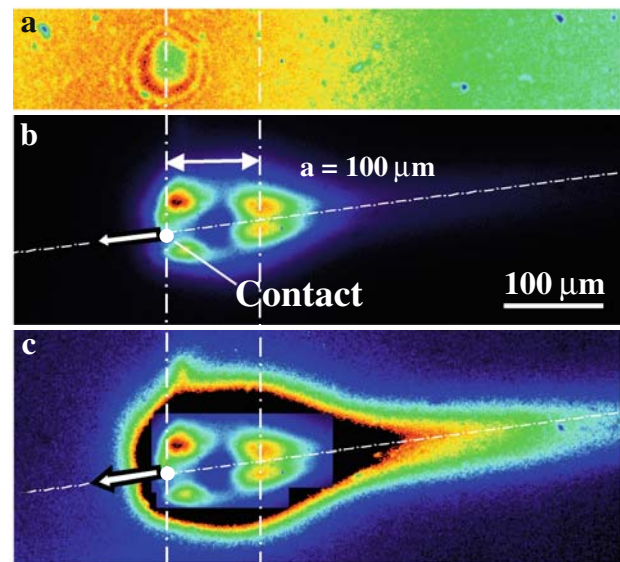


Fig. 6 Optical microscopic image measured under $F_N = 0.5$ N after the sliding experiment under light illumination (a), effective photon image (b), and composite photon image (c) measured in the dark during sliding of a diamond pin with a tip radius of $r = 1.5$ mm on a rotating MgO disk under $F_N = 0.5$ N and $V = 32$ cm/s in dry air

the effective image is overlapped onto a greater photon image, where weak photon emission was displayed at a given level, enough to show the tailing occurrence. Wear was very small also in Mg, so a clear contact Hertzian circle was formed after the sliding experiment, as shown in Fig. 6a. It is seen that the photons are emitted intensely from four strong emission points as observed in Al_2O_3 . The zone of the four points connected each other surrounding a dark zone to form a ring. The distance between the sliding contact and the center of the plasma for MgO was $a = 100$ μm as in Al_2O_3 , to also give a gap distance of $d_T = 3.3$ μm .

Figure 7 (above) shows optical microscopic images of the contact points measured under $F_N = 0.5$ N after the sliding experiment in light illumination, while Fig. 7 (below) shows the effective images of UV, visible, 696-nm, and IR photons emitted under the same experimental condition as in Fig. 6. It is seen that the effective photon images were so weak compared to those in Al_2O_3 that the plasma ring formation is not clear.

Then, the peripheral weak photon emission zones in Fig. 7 were displayed to a level sufficient to show the tailing occurrence for UV, visible, 696-nm, and IR photons in Fig. 8. The black zones in the center of the images show the photon emission intensity beyond the red levels in each image. However, no plasma ring was observed in any of the images. One of the possibilities for no observation of rings in these photon images is that they are measured through the filters, so the photon emission intensity might not be enough to show the ring. However, we need further

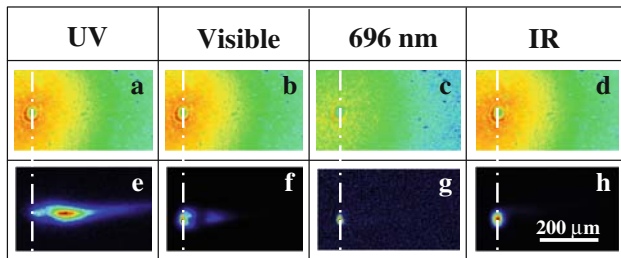


Fig. 7 Upper figures show optical microscopic images of the contact before the sliding experiment under light illumination; lower figures show effective two-dimensional images of photons emitted during sliding of a diamond pin with a tip radius of $r = 1.5$ mm on a rotating MgO disk under $F_N = 0.5$ N and $V = 32$ cm/s in dry air

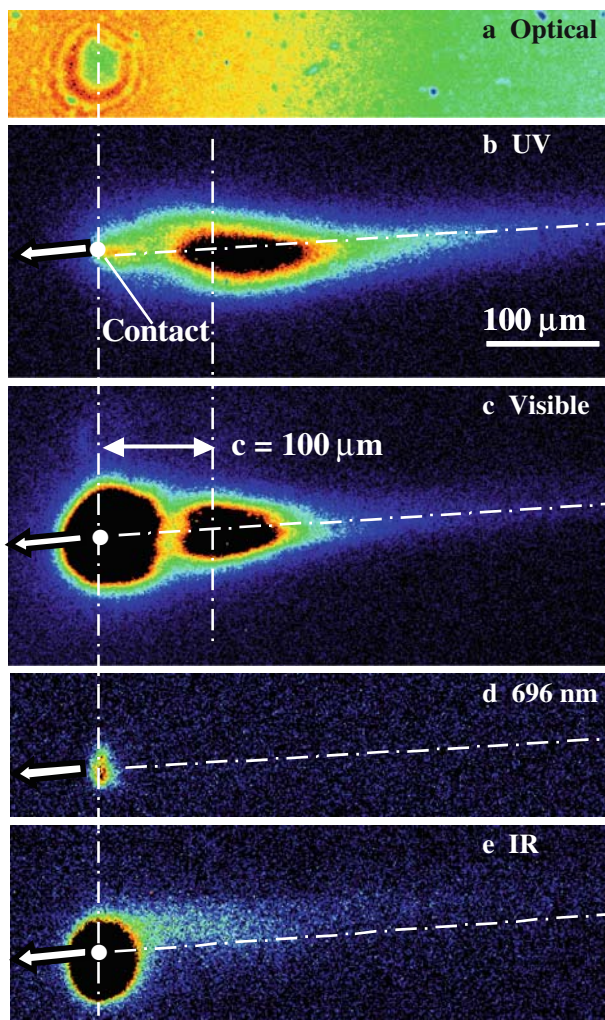


Fig. 8 Optical microscopic image after the sliding experiment (a), two-dimensional images of UV (b), visible (c), 696-nm (d), and IR (e) photons, emitted during sliding of a diamond pin with a tip radius of $r = 1.5$ mm on a rotating MgO disk under $F_N = 0.5$ N and $V = 32$ cm/s in dry air

work on this matter. Only the UV and visible images have strong photon emission regions in the rear part of the sliding contact. The distance between the contact point and

the local point of the intense plasma generation is $c = 100$ μm , which is the same value as observed for the major axis of Al_2O_3 , $a = 100$ μm .

It is noted that the UV image has a long tailing in MgO. This is one of the important different points from the characteristics of Al_2O_3 , where no tailing was observed. This suggests that the surface atoms are excited by the plasma to emit UV photons, as observed in 696-nm photons in Al_2O_3 , though we do not definitely find new peaks in the energy spectrum of the UV region in MgO. On the other hand, the visible, 696-nm, and IR photon emissions were strongest at the sliding contact, but tailing was observed only in the visible and IR images. The visible photon tailing is suggested to be caused also by excitation due to the bombardment of the active particles in the plasma. The image of the 696-nm photons at the sliding contact should be attributed to that in the broad peak in the visible region, so that the mechanism of emission differs from that in Al_2O_3 . The mechanisms of visible and IR photons will be discussed below.

3.3 SiO_2

Figure 9 shows the energy spectrum of photons emitted while sliding a diamond pin against a SiO_2 single-crystal (quartz) disk. In this solid, the energy spectrum of air-discharge plasma appeared also in the UV region, demonstrating that triboplasma is generated in this solid. However, no 696-nm sharp peak appeared in SiO_2 as in MgO. This confirms again that the 696-nm sharp peak is a characteristic of Al_2O_3 . In SiO_2 a broad band appeared also in the visible and IR regions, as in MgO. The intensity of the broad band is strongest in SiO_2 of all three kinds of solids, giving an intensity order of $\text{SiO}_2 > \text{MgO} > \text{Al}_2\text{O}_3$.

Figure 10 (above) shows optical microscopic images measured under $F_N = 0.5$ N after the sliding experiment under light illumination, while Fig. 10 (below) shows two-dimensional images of UV, visible, 696-nm, and IR photons emitted during the sliding of a diamond pin with a tip

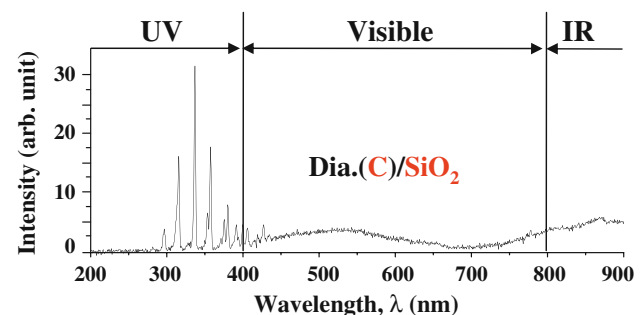
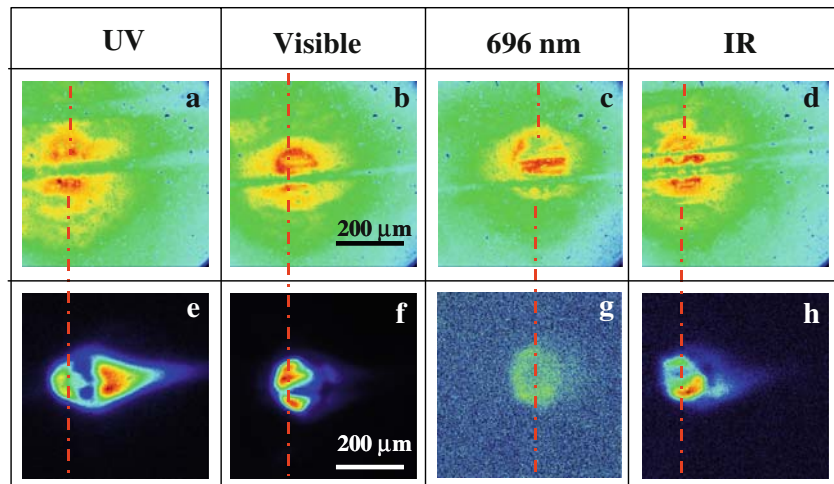


Fig. 9 Energy spectrum of photons emitted during sliding of a diamond pin with a tip radius of $r = 1.5$ mm on a rotating SiO_2 disk under $F_N = 1.0$ N and $V = 32$ cm/s in ambient air with RH = 72%

Fig. 10 Upper figures show optical microscopic images of the contact measured after the sliding experiment in light illumination and lower figures show effective two-dimensional images of photons emitted during sliding of a diamond pin with a tip radius of $r = 1.5$ mm on a rotating SiO_2 disk under $F_N = 0.5$ N and $V = 32$ cm/s in dry air in the dark



radius of $r = 1.5$ mm against an SiO_2 single-crystal disk in dry air in the dark. The SiO_2 disk was heavily damaged by wear as seen in the above figures. This high wear resulted in a change of contact geometry to give complicated two-dimensional images of UV, visible, 696-nm, and IR photons as seen in the figures below. This geometry change made the plasma ring formation difficult to be distinguished in SiO_2 .

To confirm whether a plasma ring is formed in SiO_2 or not, an additional experiment was performed with a diamond pin having a larger tip radius of $r = 3$ mm sliding against a SiO_2 single-crystal disk under $F_N = 0.5$ N and $V = 32$ cm/s in dry air in the dark. Figure 11a and c shows an optical microscopic image of the Hertzian contact and wear track measured before and after the sliding experiment in light illumination, respectively, while Fig. 11b shows a two-dimensional image of all photons detected during the sliding in the dark. An elliptical plasma ring was clearly produced as seen in Fig. 11b in the rear part of the sliding contact having a horseshoe pattern as observed in Al_2O_3 , even though the SiO_2 disk was heavily damaged by wear. This image demonstrates that a triboplasma ring was also formed in SiO_2 , as in Al_2O_3 and MgO . The plasma ring is elongated in the direction perpendicular to the sliding, in this case with $a = 140$ μm , while the distance between the center of the contact and the center of the horseshoe is $c = 122$ μm , which corresponds to the gap distance, $d_T = 2.5$ μm . In this work, the value of the tribological gap distance was observed to be $d_T = 3.3$ μm and $d_T = 2.5$ μm , respectively, for the tip radii of $r = 1.5$ and $r = 3$ mm.

The above figures in Fig. 12a–d show two-dimensional images measured during sliding in the dark for UV, visible, 696-nm, and IR photons under the same experimental condition as that in Fig. 11, while the (below) figures in Fig. 12a–d show optical microscopic images measured after the sliding experiment in light illumination. It is seen that an elliptical plasma ring is formed in the case of UV, visible,

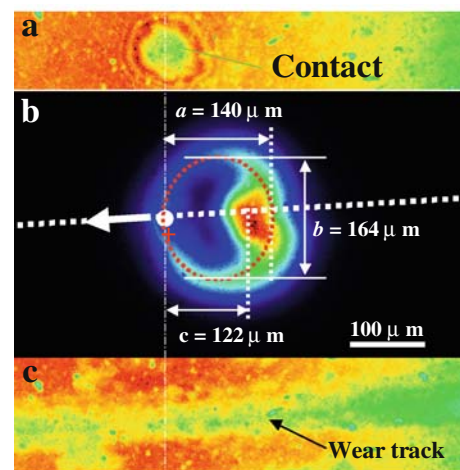


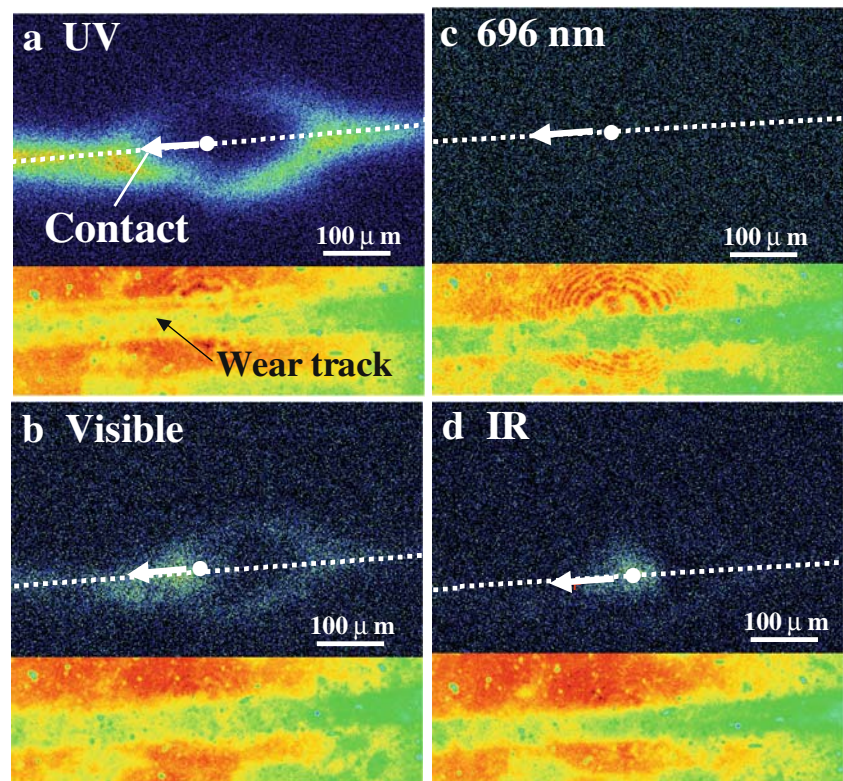
Fig. 11 Top (a) and bottom (c) figures show optical microscopic image of the contact before and after the sliding experiment, respectively, under light illumination; middle figure (b) shows effective two-dimensional image of all photons emitted during sliding of a diamond pin with a tip radius of $r = 3.0$ mm on a rotating SiO_2 disk under $F_N = 0.5$ N and $V = 32$ cm/s in dry air

and IR photons, elongated in the sliding direction, though no substantial image of the 696-nm photon was observed. The intensity of the plasma ring images decreased in the order of UV > visible > IR. It is noted that photons are emitted also in front of the sliding contact with UV, visible, and IR photons along the wear track. The reason is not clear. We need further work on this matter in relation to the wear track formation. The emission mechanisms of UV, visible, and IR photons will be discussed below.

4 Discussion

It has been shown above that in all the three kinds of disk specimens of Al_2O_3 , MgO , and SiO_2 single crystals,

Fig. 12 Effective two-dimensional images (above) of photons emitted during sliding of a diamond pin with a tip radius of $r = 3.0$ mm on a rotating SiO_2 disk under $F_N = 0.5$ N and $V = 32$ cm/s in dry air in the dark and optical microscopic images (below) measured after the sliding experiment in light illumination, for UV (a), visible (b), 696-nm (c), and IR photons (d)



triboplasma is generated emitting UV photons having a ring with the different patterns due to discharging of the ambient air by the intense electric fields of tribocharging. In the static discharging in parallel electrodes, breakdown of gas occurs at a spark voltage V_s inherent to gas. Due to the *Paschen's law*, the relation between the V_s and pd_s gives a minimum spark voltage $(V_s)_m$ at which gas sparking takes place most easily, where p and d_s are the gas pressure and the electrode distance. In the case of air under the atmospheric pressure of 1.0×10^5 Pa, the value d_s is $7.5 \mu\text{m}$ at the electric field of 4.4×10^5 V/cm for the parallel electrodes [29]. The gap distances $d_T = 2.5$ and $3.3 \mu\text{m}$ in the dynamic tribocontact in the present study are fitted well to the electrode distance of $d_s = 7.5 \mu\text{m}$ in the static air-discharge plasma [30]. This suggests that at least the same orders of magnitude as the electric strength of 4.4×10^5 V/cm in the static discharge should be generated also in the gap of sliding contact in the present study.

In this chapter, the emission mechanisms of the 696-nm, visible, and IR photons will be discussed for the three kinds of disks of Al_2O_3 , MgO , and SiO_2 , based on the already-known luminescence mechanisms, since some of the established luminescence mechanisms seem to be concerned with the origin of the 696-nm, visible, and IR photon emissions in the present work. Such luminescence is the photoluminescence (PL), cathodoluminescence (CL), thermoluminescence (TL), chemiluminescence (Chemi-L), and fractoluminescence (FL). This is because the UV

photons and electrons emitted from the triboplasma irradiate the disk surface to cause the above PL and CL, respectively, whereas the frictional temperature rise may also cause the thermal photon emission such as TL and blackbody radiation. There is a possibility also that the reaction of the fresh worn surface with the ambient molecules and the propagation of cracks in the brittle solids in the process of wear at the sliding contact cause the Chemi-L and the FL, respectively.

In discussing the CL mechanism below, it is important to know which solid surface of the pin and the disk charges negatively or positively due to the tribocharging phenomena, since the electrons attack positively charged surface to cause the CL. So, the surface potential caused by the tribocharging was measured using a noncontacting-type surface potential measuring apparatus (Trek Japan, Electric voltmeter model 334) [31] and found that the frictional track surface on the disk of all the three kinds of solid Al_2O_3 , MgO , and SiO_2 charged negatively against the diamond pin in ambient air.

4.1 Luminescence Mechanism in Single Crystal Al_2O_3

Figure 13a–c shows the spectra of photons emitted while sliding the diamond pin against the Al_2O_3 , MgO , and SiO_2 disks, whereas Fig. 13d shows the spectrum of photons emitted from the air-discharge plasma. These spectra are the ones, in which the ordinates of the above Figs. 2, 5 and

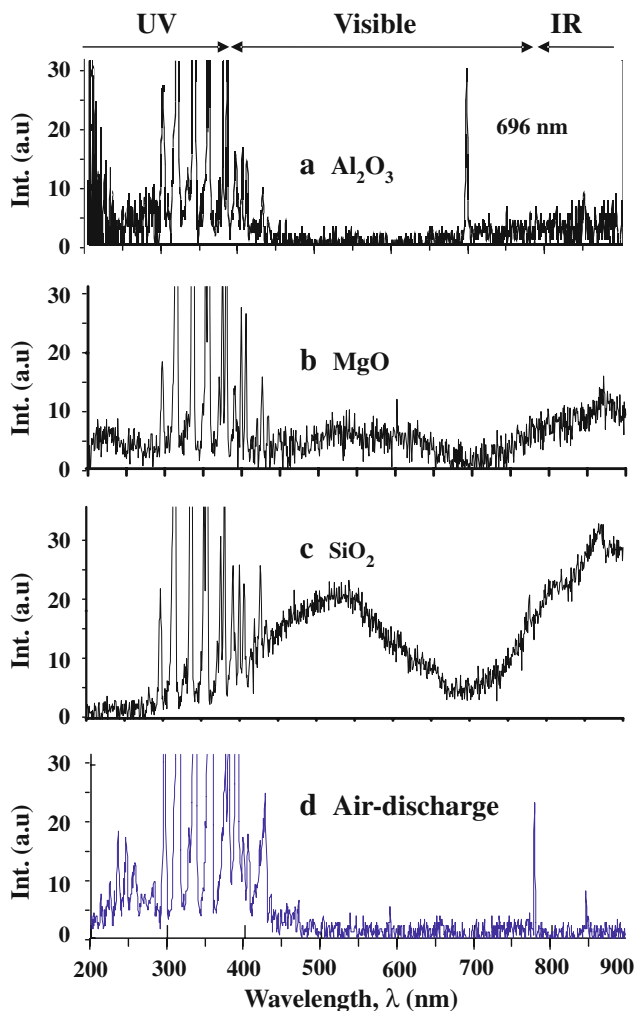


Fig. 13 Energy spectrum of photons emitted during sliding of a diamond pin on a rotating Al_2O_3 (a), MgO (b), and SiO_2 (c) disks in ambient air with a relative humidity of $\text{RH} = 40, 72,$ and 72% , respectively, under $F_N = 1.0$ N and $V = 32$ cm/s and that emitted from air-discharge plasma between a steel needle and a steel flat disk at an electrode distance of 0.3 mm in ambient air with $\text{RH} = 40\%$ (d)

9 were enlarged to see the shape of the spectra in the visible and IR regions in more detail. The narrow band at 696-nm in the Al_2O_3 disk in Fig. 13a has been attributed to a characteristics of the surface of Al_2O_3 , since the band is not seen in the spectra of MgO and SiO_2 disks as seen in Fig. 13b and c, respectively. However, the precise mechanism has not yet been clarified. So the emission mechanism of the 696-nm photons will be discussed below.

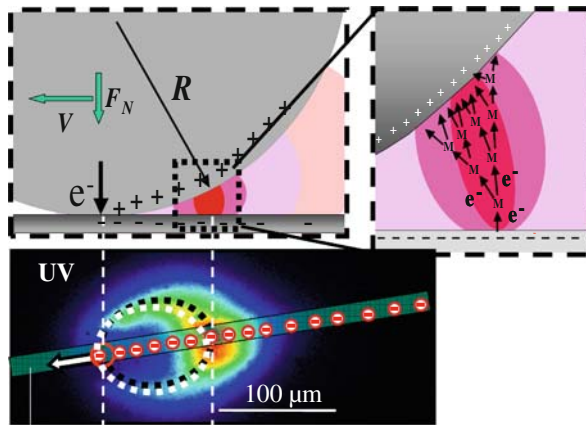
The ring of the 696-nm image overlaps to that of the UV image as seen in the comparison of Fig. 4a with c. This suggests that the 696-nm photons were emitted from the surface defect and/or impurity centers excited by the UV photons from the plasma. On the other hand, various narrow PL bands near 696-nm , which were attributed to the Cr^{3+} impurity centers, have been reported in Al_2O_3 so far under

the irradiation of UV photons. The well-known solid-state ruby laser emits the PL photons at 694.3 nm (R -line), which is emitted from the Cr^{3+} impurities doped into the single crystal Al_2O_3 . Further, a strong narrow PL band near the 696-nm due to Cr^{3+} impurities was observed at 698 nm in the nominally pure synthetic sapphire [32] and at ~ 694 nm in the ceramic Al_2O_3 prepared from the mixture of Al_2O_3 and Cr_2O_3 powders [33]. The intensity and the position of the narrow band changed depending on the Cr^{3+} ion concentration [33] and the residual stress, respectively [34]. The narrow PL Cr^{3+} band appears sometimes in doublet, for example, at 692.9 nm (R_2 -line) and 694.3 nm (R_1 -line) [35]. The Cr^{3+} impurities can give a remarkable PL band even at the concentrations of few parts per million [36]. As described above, the present Al_2O_3 disk contains $\text{Cr} < 2$ ppm. So, the narrow band at 696-nm in the present study seems to be emitted from the Cr^{3+} impurities excited by the UV photons from the triboplasma.

However, the 696-nm photon emission is not strongest at the crossing point of the plasma ring and the frictional track, at which the UV photon emission is most intense, but is strong at the pair points facing each other across the friction track as seen in Fig. 4c and d.

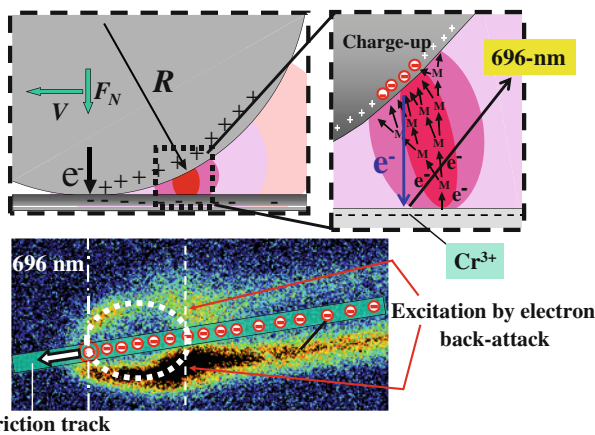
On the other hand, a narrow band has also been reported near 696-nm under the electron irradiation. A CL band at 694.4 nm due to Cr^{3+} impurities was observed in nominally pure monocrystalline corundum (Al_2O_3) [37]. The doublet R_1 and R_2 narrow bands in PL were also observed in CL in $\alpha\text{-Al}_2\text{O}_3$ single ruby crystal doped with Cr^{3+} (~ 500 ppm) [38]. These results suggest that the 696-nm band was also originated from the Cr^{3+} impurities in Al_2O_3 excited by the electrons from the triboplasma. However, the Al_2O_3 disk charges negatively and the diamond pin charges positively, so that the electrons attack the positively charged diamond, and no CL narrow band was reported at 696-nm in diamond.

Then, why the 696-nm photon emission is weak on the frictional track and strong at the two pair points facing each other across the frictional track? One of the possible explanations is as follows. First the electrons emitted from the negatively charged frictional track surface bombard the positively charged dielectric diamond pin surface (see Fig. 14), and then the electrons are accumulated in local areas of the diamond pin surface to produce strong negatively charged patches (see Fig. 15). The negative patches generate extremely intense local inverse electric fields directing from the negatively charged diamond surface patches to the Al_2O_3 disk surface. Then the electrons are accelerated inversely toward the sapphire disk surface. However, the original frictional surface, at which the electrons were emitted, is charged negatively, so that the electrons are repelled from the negatively charged frictional track surface to bombard just outside the track. Then



Friction track

Fig. 14 Model of electron avalanche process



Friction track

Fig. 15 Model of electron back-attack process

the CL photons are emitted from the Cr^{3+} ions excited by the back electrons at the two pair points. Figure 15 shows the mechanism of the photon emission from the Cr^{3+} ions excited by the back-electron irradiation at the two pair points facing each other across the friction track. This is a possible mechanism why the two pair points were intense just outside of the frictional track in the 696-nm photon image in Fig. 4c and d. As the 696-nm photons were also emitted at the frictional track, both the PL and CL photons probably contributed to the 696-nm photon emission in the present study. The length of the tails originated from the pair points are longer than 200 μm , which corresponds to the life time $\tau > 0.6$ ms. Namely the excited Cr^{3+} ion center has the life time longer than 0.6 ms.

When we compare the spectrum of the tribophotons and that of the air-discharge photons shown in Fig. 13a and d, respectively, we notice that the tribophoton emission in the visible and IR regions are composed of the narrow band at about 425 nm due to the air-discharge plasma, the low photon emission in the wavelength region 450–700 nm due

to the air discharge, the 696-nm photon emission from the excited Cr^{3+} ions, and the photon emission in the wavelength region 700–800 nm, which should be composed of the low photon emission from the plasma and the tribophoton emission which increases with the increase in the wavelength. The strong photon emission at the pair points facing each other across the wear track are more clearly seen in the visible photon image in Fig. 4b. The main visible photons at the pair points should be due to the 696-nm CL photons emitted from the Cr^{3+} centers excited by the electrons.

The photon emission in the wavelength region 700–900 nm seems to be originated from the thermal emission probably due to the black body radiation caused by the frictional temperature rise, combined with the weak photon emission from the plasma. The two narrow bands in the wavelength region 700–900 nm in the gas-discharge spectrum are noises. So, the IR photon emission should be composed of the thermal emission caused by the frictional temperature rise at the sliding contact and that emitted from the plasma.

Fractoluminescence at the sliding contact and chemiluminescence [39] can be neglected since the wear of the Al_2O_3 disk is negligibly small.

4.2 Luminescence Mechanism in Single-Crystal MgO

The photon energy spectrum in the visible and IR regions in the MgO disk is composed of a narrow band at about 425 nm due to the air discharging, a broad band in the wavelength region 450–700 nm consisting of various narrow bands peaked at about 530 nm, and a broad band 700–900 nm peaked at about 870 nm as seen in Fig. 15b. In the MgO disk, the plasma ring and the two pair points facing across the friction track were also observed as seen in Fig. 6. Based on the photon energy spectra in Fig. 13b and d and the photon images in Fig. 8, the UV, visible, 696-nm, and IR photon emission mechanisms are discussed below.

The visible photon image in the rear part of the sliding contact overlaps to the UV image as seen in the comparison of Fig. 8b with c. This suggests that the visible photons were emitted from the defects and/or impurities excited by the UV photons and/or the electrons from the plasma as in the Al_2O_3 disk.

It is known that deformation of solid produces defect centers. Walter et al. identified the defects formed by the deformation of MgO to F^+ and F centers, which are the oxygen ion vacancies containing one and two electrons, respectively [40], whereas Wertz et al. identified also the defects formed by the neutron irradiated MgO to the F^+ and F centers [41]. The deformation centers emit PL photons giving bands at about 400 nm and at about 520 nm in MgO, in which the band at about 400 nm was attributed

to the F^+ center, whereas the one at about 520 nm to the F centers, respectively [42–46]. Dickinson et al. showed that the intensity of the broad band at around 400 nm increases in the order of abrasion > polishing > cleaving, i.e., in the order of the number of the defect formation [47]. On the other hand, Duley et al. observed a PL band at 560 nm, which was originated from other source than the F-centers, a broad PL band at 610 nm originated from Fe^{3+} ions, and a narrow PL band at 700 nm due to Cr^{3+} impurities [48]. As the present MgO specimen surface was mechanically polished, the surface outside the wear track should also have the deformed defect centers in addition to the wear track surface and the specimen contains also Fe impurities in 140 ppm as described above. So, the visible photon emission in the broad band from 400 to 700 nm in the present work probably is due to the defects of F and F^+ centers and Fe impurities excited by the plasma UV photons. The negligible small content of Cr in the present test specimen corresponds also well to the negligible photon emission intensity at 710 nm originated from Cr^{3+} ions.

On the other hand, Llopis et al. successfully took a CL image of the defects formed by the deformation of MgO [49], whereas Datta et al. observed the two overlapping CL bands which peaked at 425 and 488 nm in the wavelength range 300–650 nm and a broad CL band, which peaked at 466 in the wavelength range 350–600 nm before and after the deformation of MgO, respectively. In the near IR region, they further observed a broad CL band consisting of a number of unresolved peaks in the wavelength range 650–830 nm in the undeformed MgO, the strongest which was at 726 nm due to Fe impurities [50]. As the present MgO specimen should have contained the deformed defects on the surface due to the mechanical surface finishing and wear and contained the Fe impurities in 140 ppm as described above, these reports strongly suggest that the two kinds of pair points across the frictional track seen in Fig. 6 were originated from the deformed defects and Fe impurities excited by the electron back attack as observed in the Al_2O_3 disk, though the two facing points across the frictional track are not clearly seen in the visible photon image in Fig. 8c.

The visible, 696-nm, and IR photons were most intense in the sliding contact as seen in Fig. 8c–e. It has been reported that a broad TL band appeared at about 540 nm during heating of MgO at above room temperature. The emission mechanism was suggested to be due to F-type centers associated with Fe impurity traps [51]. So, the broad TL band at 540 nm probably contributed to the strong visible photon emissions at the sliding contact due to the frictional temperature rise. In the wavelength region 700–900 nm, the photon emission was increased with the increase in the wavelength as in the Al_2O_3 disk. The photon emission at the sliding contact should also be due to another thermal emission by the blackbody radiation

caused by frictional temperature rise. The 696-nm photon emissions at the sliding contact should be a part of the thermal emission caused by frictional heating.

A strong MgO fractoemission band was reported at 730 nm in the wavelength range 600–900 nm, which was originated from Cr impurities, as well as weak emission bands from 400 to 500 nm [52]. However, no strong broad emission band centered at 730 nm is seen in Fig. 13b, Cr impurity was negligible and wear also extremely small in the present specimen. So the luminescence due to the fractoluminescence at the sliding contact should be neglected. Chemi-luminescence should also be neglected because of the negligibly small wear.

4.3 Luminescence Mechanism in Single-Crystal SiO_2

The photon energy spectrum in the visible and IR regions in the SiO_2 disk is composed of a narrow band at about 425 nm due to air discharge, a broad band from 450 to 700 nm peaked at around 530 nm, and a broad band from 700 to 900 nm, the intensity of which increases with the increase in the wavelength as in the Al_2O_3 and MgO disks as seen in Fig. 13c. No pair points were seen facing each other across the wear track in all the photon images of the total, UV, visible 696-nm, and IR photons, whereas the photon emission is strongest at the crossing points of the plasma ring and the wear track as seen in Figs. 11 and 12.

The MgO disk was worn out heavily, so that a clear wear track was formed. This means that a lot of luminescence defect centers were produced along the wear track due to the Si–O bond scission ($\equiv Si-O-Si \equiv \rightarrow \equiv Si \bullet + \bullet O-Si \equiv$) caused by the wear and fracture of brittle SiO_2 at the sliding contact. The $\equiv Si \bullet$ and $\bullet O-Si \equiv$ are called E' center and NBOHC (nonbridging oxygen hole center), respectively. Both the E' and NBOH are the well-known centers for PL and CL. Oxygen vacancies and interstitial oxygen atoms should also be created in the two ways in the wear process, (1) by reconstruction of the two neighboring E' centers ($\equiv Si-O-Si \equiv \rightarrow \equiv Si \bullet + \bullet O-Si \equiv \rightarrow \equiv Si \bullet + \bullet Si \equiv + O \rightarrow \equiv Si-Si \equiv + O$ (interstitial)) and (2) knock-on of the oxygen atom ($\equiv Si-O-Si \equiv \rightarrow \equiv Si-Si \equiv + O$ (interstitial)) [53].

The UV photons were emitted along the wear track before the sliding contact, in addition to the photon emission along the wear track after the plasma ring as seen in Fig. 12a. The UV photon emission before the sliding contact is difficult to be explained with the air-discharge mechanism, since the intense tribocharge-electric field to cause air discharge is generated in the rear gap of the sliding contact. Jones et al. observed CL bands in the UV region at 260 nm (4.77 eV) in crystalline SiO_2 and 290 nm (4.28 eV) in amorphous SiO_2 . These bands were correlated with the oxygen vacancies in the optical and spin resonance

measurements [54]. However, it is difficult to find these bands in Fig. 9. So, we need further work for clarifying the UV photon emission mechanism along the wear track.

The visible photon image overlapped completely to the UV one as seen in Fig. 12a and b. This suggests that the visible photons are emitted by the PL mechanism due to the UV photon irradiation and/or the CL mechanism by the electron irradiation from the triboplasma as in the Al_2O_3 and MgO disks. Skuja et al. observed PL bands at about 2.65 eV (~ 468 nm) and 1.9 eV (652 nm) in amorphous SiO_2 [55]. The 2.65 band was attributed to triplet-to-singlet transitions in silicon-related intrinsic defects [56], whereas the bands at about 1.9 eV to the transition between the two atomic type $2p$ orbitals in a lone pair and an unpaired electron in the NBOHCs of SiO_2 [57]. On the other hand, a PL broad band at 530 nm was observed in SiO_2 prepared by sol-gel processing under excitation with Ar^+ laser (488 nm). This band was attributed to the defects in SiO_2 such as $\equiv\text{Si}\cdot$ (E' center) and $\bullet\text{O}-\text{Si}\equiv$ (NBOHC). [57]. These previous reports suggest that the present broad visible band peaked at 530 nm arose from the defects such as E' centers and NBOHCs in SiO_2 excited by the irradiation of UV and visible photons emitted from the triboplasma.

On the other hand, some CL bands from the defect centers in SiO_2 were also reported in the visible wavelength region 430–650 nm. They are the bands at about 450 nm observed in SiO_2 layer on Si and bulk fused silica [58], at 480 nm in fused silica, and at 460 nm in crystal quartz [59]; at 450 nm in glassy SiO_2 and at 480 nm in crystalline SiO_2 [60]; at near 2.9 eV (430 nm) and 2.5 eV (500 nm) in the crystal quartz, and at near 2.9 eV (430 nm), 2.5 eV (500 nm), 1.9 eV (650 nm) in the amorphous quartz [54]; at 450 nm accompanied with bands at 288, 559, and 637 nm in high-purity silica [61]; at 2.5 eV (496 nm) and 2.8 eV (442 nm) in quartz [62]. These bands were attributed to the E' centers, NBOHCs, oxygen vacancies, and impurities. So, the broad band centered at 530 nm in the present study is also attributable to the CL mechanism caused by the bombardment of the electrons from the triboplasma onto the luminescent centers in the SiO_2 disk surface.

However, no pair points across the wear track were observed in the SiO_2 disk, though the SiO_2 disk charged negatively. One of the possible mechanisms to be able to explain the phenomenon is as follows. In the Al_2O_3 and MgO disks in which the pair points were observed, the wear was negligibly and very small, whereas in the SiO_2 disk, the disk was heavily worn out to produce wear track as seen in Figs. 11 and 12. This suggests that the charges on the frictional track needed to repel the back electrons were continuously removed away together with the wear debris in the SiO_2 disk. This removal of the charges through the wear process weakens the surface potential on the frictional track. Then, the high-energy back electrons can easily

attack the frictional surface, so that no pair points facing across the wear track were observed in the MgO disk. This a possible mechanism. We need further work to clarify it.

At the sliding contact, the visible and IR photon emission intensity was strongest in the SiO_2 disk as in the Al_2O_3 and MgO disks. A TL band at 3.1 eV (400 nm) due to the impurities was reported in quartz and silica [63], whereas a luminescence band in the wavelength region 450–700 nm observed during cutting quartz with diamond-impregnated saw blade was attributed to blackbody radiation [64]. The photon emission in the wavelength range of 700–900 nm in the present study is probably due to the blackbody radiation caused by the frictional temperature rise and photon emission from the plasma, as in the Al_2O_3 and MgO disks. So, the visible and IR photon emissions at the sliding contact should also be originated from the thermal emission consisting of the TL and blackbody radiation due to the frictional heating.

On the other hand, Zinc et al., observed FL bands at 430 and 630 nm during crashing of silica, which were attributed to the defects of E' center and other defects produced by the mechanical action [65]. Kawaguchi observed the FL bands at 2.7 eV (459 nm) and 1.9 eV (652 nm) during fracture of silica, where the 2.7 eV band assigned to triplet-to-ground state relaxation on the oxygen vacancies, or oxygen deficient centers (ODC: $\equiv\text{Si}-\text{Si}\equiv$), whereas the 1.9 eV band was associated with the relaxation of NBOHCs [53]. He observed also the FL bands at 2.9 eV (429 nm) and 2.0 eV (620 nm) in quartz. The 2.9 eV band was attributed to relaxation luminescence ODC, while the 2.0 eV band was not to NBOHCs but to an impurity center possibly Na or Li center [66]. So, there is a possibility that the FL contributed to the visible photon emission in addition to the thermal emission at the sliding contact in the present study. Chemiluminescence should be omitted since SiO_2 is so chemically stable to react with air. However, we need further work for clarifying the photon-emission mechanism in the sliding contact in the SiO_2 disk.

As seen in Fig. 13, the photon emission intensity in the wavelength region 700–900 nm increased in the order of $\text{SiO}_2 > \text{MgO} > \text{Al}_2\text{O}_3$. This trend should be concerned with the parameters concerned with the frictional temperature rise such as thermal conductivity of these solids. In the MgO and SiO_2 disks, the visible photons in the wavelength region 450–700 nm are emitted from defect centers produced by deformation, so that the photon emission intensity in this region should depend on the extent of the surface deformation caused by wear.

5 Conclusions

To know how sliding solid species of a stationary sliding partner affects plasma generation, the energy spectrum and

two-dimensional distribution of photon emission were investigated during the sliding of a diamond pin with a tip radius of 1.5 and 3 mm on three kinds of solid species—sapphire (Al_2O_3), magnesium oxide (MgO), and quartz (SiO_2)—of the stationary sliding partners in dry sliding in air, and the following conclusions have been drawn.

- (1) It has been confirmed that the triboplasma is generated by discharging of the ambient gas due to the intense electric field caused by tribocharging without depending on the kinds of the insulating stationary sliding partner as observed in the Al_2O_3 , MgO , and SiO_2 disks in the present study.
- (2) The emission regions of the visible photon, which have one or two tailings, overlapped to those of the UV photons in all stationary solid tested. The visible photons should be emitted from the defect and/or impurity centers excited by the UV photons and electrons from the triboplasma as well as those from the triboplasma itself.

The visible photon emission in Al_2O_3 is characterized by a strong narrow band at 696-nm. The 696-nm band was attributed to the Cr^{3+} impurities in Al_2O_3 excited by the photons and electrons from the triboplasma. The visible photon emission in MgO should be mainly due to the F and F^+ centers, which are the oxygen ion vacancies containing one and two electrons, and Fe impurities excited by the UV photons and electrons from the triboplasma. The visible photon emission in SiO_2 probably arises from the E' centers, NBOHCs , oxygen vacancies excited by the UV photons, and electrons from the triboplasma.

- (3) The visible photon emission was found to be most intense at the pair points facing each other across the frictional track in Al_2O_3 and MgO , in spite of that the UV photon emission was strongest at the crossing point of the plasma ring and the wear track. The photon emission at the pair points in Al_2O_3 and MgO was attributed to the cathodoluminescence caused by the back attack of the electrons, which are accelerated by the inverse electric field caused by the negatively charged patches formed on the diamond pin surface by the electron bombardment, to the disk surface. In this process, the electrons are repelled from the negative charge of the frictional track, so that the electrons attack the two pair points just outside the frictional track avoiding the negative frictional track.
- (4) The IR photon emission should be composed of thermoluminescence from the defects and impurity centers and/or blackbody radiation due to frictional temperature rise at the sliding contact and the photon emission from the triboplasma itself.

- (5) Fractoluminescence should have some roles in the photon emission at the sliding contact in such insulating brittle solids as in SiO_2 , where heavy wear takes place.

Acknowledgment This work was supported by KAKENHI (Grant-in-Aid for Scientific (A)20246035).

References

1. Archard, J.F.: The temperature of rubbing surface. *Wear* **2**, 438–455 (1958/1959)
2. Iluc, I.: *Tribology of Thin Layers*. Elsevir, New York (1980)
3. Sakurai, T., Sato, K.: Study of corrosivity and correlation between chemical reactivity and load carrying capacity of oils containing extreme pressure agents. **9**, 77–87 (1966)
4. Bowden, F.P., Tabor, D.: *The Friction and Lubrication of Solids*. Clarendon, Oxford (1950)
5. Heinecke, G.: *Tribochemistry*. Verlag, Berlin (1984)
6. Mori, S., Takahashi, K., Wayama, K., Asabe, Y.: Chemisorption of ethers on nascent nickel surfaces formed under vacuum conditions at room temperature. *Proc. Int. Trib. Conf. Nagoya*, 1171–1176 (1990)
7. Kajdas, C.: On a negative-ion concept of EP action of organic-sulfur compounds. *ASLE Trans.* **28**, 21–30 (1984)
8. Karis, T.E., Novotny, V.J., Johnson, R.D.: Mechanical scission of perfluoropolyethers. *J. Appl. Polym. Sci.* **50**, 1357–1368 (1993)
9. Nakayama, K., Leiva, J.A., Enomoto, Y.: Chemi-emission of electrons from metal surfaces in the cutting process due to metal/gas interactions. *Tribol. Int.* **28**, 507–515 (1995)
10. Koyama, M., Hayakawa, J., Onodera, T., Ito, K., Tsubori, H., Endou, A., Kubo, M., Carpio, C.A.D., Miyamoto, A.: Tribochemical reaction dynamics of phosphoric ester lubricant additive by using a hybrid tight-binding quantum chemical molecular dynamics method. *J. Phys. Chem. B* **110**, 17507–17511 (2006)
11. Nakayama, K., Fujimoto, T.: The energy of electrons emitted from wearing solid surfaces. *Tribol. Int.* **17**, 75–81 (2004)
12. Nakayama, K., Suzuki, N., Hashimoto, H.: Triboemission of charged particles and photons from wearing solid surfaces during frictional damage. *J. Phys. D Appl. Phys.* **25**, 303–308 (1992)
13. Nakayama, K., Nevshupa, R.A.: Characteristics and pattern of plasma generated at sliding contact. *Trans. ASME* **125**, 780–787 (2003)
14. Nakayama, K.: Triboemission of charged particles and resistivity of solids. *Tribol. Int.* **6**, 37–40 (1999)
15. Lide, D.A. (ed.): *Handbook of Chemistry and Physics*. CRC (1998–1999)
16. Nakayama, K.: Tribophysical phenomena and tribochemical reaction. *Jpn. J. Tribol.* **42**(9), 1077–1084 (1997)
17. Nakayama, K., Nevshupa, R.A.: Plasma generation in a gap around a sliding contact. *J. Phys. D Appl. Phys.* **35**, L53–L56 (2002)
18. Nakayama, K.: The plasma generated and photons emitted in an oil-lubricated sliding contact. *J. Phys. D Appl. Phys.* **40**, 1103–1107 (2007)
19. Nakayama, K., Hashimoto, H.: Triboemission, tribochemical reaction, and friction and wear in ceramics under various n-butane gas pressures. *Tribol. Int.* **29**, 385–393 (1996)
20. Nakayama, K., Mirza, S.M.: Verification of the decomposition of perfluoropolyether fluid due to tribomicroplasma. *Tribol. Trans.* **49**, 17–25 (2006)

21. Nakayama, K.: Triboemission and triboplasma generation with DLC films. In: Donnet, C., Erdemir, A. (eds.) *Tribology of Diamond-Like Carbon Films*. Springer (2008)
22. Nakayama, K., Nevshupa, R.A.: Effect of dry air pressure on characteristics and pattern of triboplasma. *Vacuum* **74**, 11–17 (2004)
23. Nakayama, K., Hashimoto, H.: Effect of surrounding gas pressure on triboemission of charged particles and photons from wearing ceramic surfaces. *Tribol. Trans.* **38**, 35–42 (1995)
24. Nakayama, K.: Contact geometry and distribution of plasma generated in the vicinity of sliding contact. *Jpn. J. Appl. Phys.* 6007–6014 (2007)
25. Haper, W.R.: *Contact and Frictional Electrification*. Clarendon (1967)
26. Latham, J.: Electrification produced by the asymmetric rubbing of ice on ice. *J. Appl. Phys.* **14**, 488–490 (1963)
27. Oguchi, T., Tamatani, M.: Contact electrification in inorganic binary compounds. *J. Electrochem. Soc.* **133**, 841–847 (1986)
28. Kornfeld, M.I.: Frictional electrification. *J. Phys. D Appl. Phys.* **9**, 1183–1192 (1976)
29. Nakayama, K., Hashimoto, H.: Triboemission of charged particles and photons from wearing ceramic surfaces in various gases. *Tribol. Trans.* **35**, 643–650 (1992)
30. von Engel, A.: *Ionized Gases*. AIP, New York (1992)
31. Nakayama, K.: Tribocharging and friction in insulators in ambient air. *Wear* **194**, 185–189 (1996)
32. Kristianpoller, N., Rehavy, A.: Luminescence center in Al₂O₃. *J. Lumin.* **18/19**, 239–243 (1979)
33. Toyoda, T., Obikawa, T., Shigenari, T.: Photoluminescence spectroscopy of Cr³⁺ in ceramic Al₂O₃. *Mater. Sci. Eng.* **B54**, 33–37 (1998)
34. Pan, Chennan., Chen, S., Shen, P.: Photoluminescence and transformation of dense Al₂O₃: Cr³⁺ condensates synthesized by laser-ablation route. *J. Cryst. Growth* **310**, 699–705 (2008)
35. Patra, A., Tallman, R.E., Weinstein, B.A.: Effect of crystal structure and dopant concentration on the luminescence of Cr³⁺ in Al₂O₃ nanocrystals. *Opt. Mater.* **27**, 1396–1401 (2005)
36. Nagabhushana, H., Umesh, B., Nagabhushana, B.N., Lakshminarasappa, B.N., Singh F., Chakradhar, R.P.S. Photoluminescence studies of 100 MeV 8+ ion irradiated Al₂O₃ single crystals. *Spectrochim. Acta A: Mol. Biomol. Spectrosc.* (2008) accepted
37. Milman, I.I., Moiseykin, E.V., Nikiforov, S.V., Mikhailov, S.G., Solomonov, V.I.: Luminescence properties of α -Al₂O₃ dosimetric crystals exposed to a high-current electron beam. *Radiat. Meas.* **38**, 443–446 (2004)
38. Mkhov, V.N., Lusichik, A., Lushichik, Ch.B., Kirm, M., Vasilchenko, E., Vierhauer, S., Harutunvan, V.V., Aleksanvan, E.: Luminescence and radiation defects in electron-irradiation defects in electron defects in electron-irradiated Al₂O₃ and Al₂O₃: Cr. *Nucl. Instrum. Meth.* **B266**, 2949–2952 (2008)
39. Kasemo, B., Toernqvist, E., Wallden, L.: Metal-gas reactions studied by surface chemiluminescence. *Mater. Sci. Eng.* **42**, 23–29 (1980)
40. Walters, G.K., Estle, T.L.: Paramagnetic resonance of defects introduced near the surface of solids by mechanical damage. *J. Appl. Phys.* **32**, 1854–1859 (1961)
41. Wertz, J. E., Auzins, P., Weeks, R. A.: Electron spin resonance of f centers in magnesium oxide; confirmation of the spin of magnesium-25. *Phys. Rev.* **107**, 1535–1537 (1957)
42. Chen, Y., Kolopus, J.L., Sibley, W.A.: Luminescence of the F⁺ center in MgO. *Phys. Rev.* **186**, 865–870 (1969)
43. Kapper, L.A., Kroes, R.L., Henseley, E.B.: F⁺ and F, centers in magnesium oxide. *Phys. Rev.* **1**, 4151–4157 (1970)
44. Chen, Y., Kolopus, J.L., Sibley, W.A.: Defect luminescence in irradiated MgO. *J. Lumin.* **1**, 633–640 (1970)
45. Williams Jr., G.P., Rosenblatt, G.H., Ferry, M.J., Willias, R.T., Chen, Y.: Time resolved luminescence and absorption spectroscopy of defects in MgO and Al₂O₃. *J. Lumin.* **40&41**, 339–340 (1988)
46. Rosenblatt, G.H., Rowe, M.W., Williams Jr., G.P., Williams, R.T.: Luminescence of F and F+ centers in magnesium oxides. *Phys. Rev.* **39**, 10309–10318 (1989)
47. Dickinson, J.T., Jensen, L.C., Webb, R.L., Langford, S.C.: Photoluminescence imaging of mechanically produced defects. *J. Non-Cryst. Solids* **177**, 1–8 (1994)
48. Duley, W.W., Rosatzin, M.: The orange luminescence band in MgO crystals. *J. Phys. Chem. Solids* **46**, 165–170 (1985)
49. Llopis, J., Piqueras, J., Bru, L.: Cathodoluminescence from slip planes in deformed MgO. *J. Mater. Sci.* **13**, 1361–1364 (1978)
50. Datta, S., Boswarva, I.M., Holt, D.B.: Cathodoluminescence in deformed MgO crystals. *J. Phys. Chem. Solids* **40**, 567–571 (1979)
51. Chakrabarti, K., Mathur, V.K.: Optically and thermally stimulated luminescence in MgO. *Solid State Commun.* **77**, 481–483 (1991)
52. Kawaguchi, Y.: Luminescence spectra at bending fracture of single crystal MgO. *Solid State Commun.* **117**, 17–20 (2001)
53. Kawaguchi, Y.: Time-resolved fractoluminescence spectra of silica in a vacuum and nitrogen atmosphere. *Phys. Rev. B* **52**, 9224–9228 (1995)
54. Jones, C.E., Embree D.: Correlation of the 4.77–4.28-eV luminescence band in silicon dioxide with the oxygen vacancy. *J. Appl. Phys.* **47**, 5365–5371 (1976)
55. Skuja, L.N., Streletsky, A.N., Pakovich, A.B.: A new intrinsic defect in amorphous SiO₂: twofold coordinated silicon. *Solid State Commun.* **50**, 1069–1072 (1984)
56. Silin, A.R., Skuja, L.N., Trukhin, A.N.: Intrinsic defects generation mechanism in fused silica. *J. Non-Cryst. Solids* **38 &39**, 195–200 (1980)
57. Okuzaki, S., Okude, K., Ohishi, T.: Photoluminescence behavior of SiO₂ prepared by sol–gel processing. *J. Non-Cryst. Solids* **265**, 61–67 (2000)
58. Mitchell, Jdenure, D.G.: A study of SiO layer on Si using cathodoluminescence spectra. *Solid State Electron.* **16**, 825–839 (1973)
59. Sigel Jr., G.H.: Ultraviolet spectra of silicate glasses: a review of some experimental evidence. *J. Non-Cryst. Solids.* **13**, 372–398 (1973)
60. Sigel, G.H., Jr., Friebele, E.J., Ginther, R.J., Griscon, D.L.: Effect of stoichiometry on the radiation response of SiO₂. *IEEE Trans. Nucl. Sci.* **NS-21**, 56–61 (1974)
61. Wang, P.W., Haglund, R.F., Kinsler, D.L., Mendenhall, M.H., Tolk, N.H., Weeks, R.A.: Luminescence induced by low energy electron desorption in suprasil and spectrosil glasses. *J. Non-Cryst. Solids* **102**, 288–294 (1988)
62. Itoh, C., Tanimura, K., Itoh, N.: Optical studies of self-trapped excitons in SiO₂. *J. Phys. Solid State Phys.* **21**, 4693–4702 (1988)
63. Guzzi, M., Lucchini, G., Martini, M., Pio, F., Vedda, A., Grilli, E.: Thermally stimulated luminescence above room temperature of amorphous SiO₂. *Solid State Commun.* **75**, 75–79 (1990)
64. Chapman, G.N., Walton, A.J.: Triboluminescence of glasses and quartz. *J. Appl. Phys.* **54**, 5961–5965 (1983)
65. Zinc, J.Y., Beese, W., Schneider, J.W.: Triboluminescence of silica core optical fibers. *Appl. Phys. Lett.* **40**, 110–112 (1982)
66. Kawaguchi, Y.: Fractoluminescence spectra in crystalline quartz. *J. Appl. Phys.* **37**, 1892–1896 (1998)